Potassic igneous rocks from the vicinity of epithermal gold mineralization, Lihir Island, Papua New Guinea

Article *in* Lithos · June 2001

DOI: 10.1016/S0024-4937(01)00035-4

4 authors, including:

Leander Franz
University of Basel
66 PUBLICATIONS **1,750** CITATIONS

ELSEVIER

Lithos 57 (2001) 163–186

LITHOS

www.elsevier.nl/locate/lithos

Potassic igneous rocks from the vicinity of epithermal gold mineralization, Lihir Island, Papua New Guinea

Daniel Müller [a,*], Leander Franz [a], Peter M. Herzig [a], Steve Hunt [b]

[a] *Institut für Mineralogie, TU Bergakademie Freiberg, Brennhausgasse 14, D-09596 Freiberg, Germany*
[b] *Lihir Gold Limited, P.O. Box 789, Port Moresby, Papua New Guinea*

Received 20 July 2000; accepted 2 March 2001

Abstract

Many world-class porphyry copper–gold and epithermal gold deposits worldwide are hosted by volatile-rich and oxidized alkaline rocks. This study investigates potassic igneous rocks from the vicinity of epithermal gold mineralization at Lihir Island, Papua New Guinea. The island consists of five Pliocene–Pleistocene stratovolcanoes, one of which hosts Ladolam, one of the largest epithermal gold deposits discovered to date.

Petrographically, the rocks range from porphyritic trachybasalts, trachyandesites and latites to rare phonolites and olivine–clinopyroxene cumulates. In some places, these rocks are cut by monzodiorite stocks. According to Al-in-hornblende barometry, the main crystallization of these rocks occurred close to the surface. Titanium-in-hornblende thermometry as well as olivine–spinel geothermometry and oxygen barometry indicate temperatures of 787–965°C at elevated oxygen fugacities (f_{O_2}) of 1.4–4.8 log units above that of the FMQ buffer. Although previous studies have suggested high f_{O_2} of alkaline rocks associated with copper–gold mineralization based on abundant primary magnetite contents, this is the first direct determination of the f_{O_2} of such rocks. High f_{O_2} of parental melts commonly delays the early crystallization of magmatic sulphides; this is important because metals such as Au and Cu preferentially partition into sulphide phases resulting in their depletion in the melt during increasing fractionation.

Geochemically, the rocks range from primitive to relatively evolved compositions, as reflected by their SiO_2 (45.8–55.0 wt.%) and MgO (1.4–15.3 wt.%) contents and variable concentrations of mantle-compatible elements (130–328 ppm V, 1–186 ppm Ni). Their high K_2O content (up to 4.7 wt.%), high average K_2O/Na_2O ratios (0.8) and high average Ce/Yb ratios (14) are typical of high-K igneous rocks transitional to shoshonites. Although these rocks formed by decompression melting related to back-arc rifting in the Manus Basin, the high LILE, low LREE and very low HFSE concentrations are typical of potassic igneous rocks from oceanic (island) arc settings. The reason for this remarkable composition is the partial melting of subduction-modified lithospheric mantle, which developed in a stalled subduction zone.

Mica phenocrysts in the rocks reveal unusually high halogen concentrations. Magmatic phlogopites contain high F (up to 5.6 wt.%) and elevated Cl contents (<0.08 wt.%). Hydrothermal biotites from rocks that display potassic alteration have low F (<0.08 wt.%), but very high Cl concentrations (up to 0.15 wt.%). It is suggested that chloride complexing largely

* Corresponding author. Fax: +49-3731-392610.
E-mail address: damuell@mineral.tu-freiberg.de (D. Müller).

PII: S0024-4937(01)00035-4

controlled the abundances of Au and Cu in the aqueous fluids responsible for the hydrothermal gold mineralization at Ladolam.

Keywords: Potassic igneous rocks; Lihir Island; Geothermobarometry; Oxygen barometry; Epithermal gold mineralization; Volatiles

1. Introduction

The southwest Pacific hosts some of the world's premier gold and copper–gold deposits (Andrew, 1995). One particular example is the Ladolam gold deposit on Lihir Island in the Bismarck Archipelago, northeast of Papua New Guinea (Fig. 1). Ladolam contains a geological resource of >43 million ounces of Au, hence representing one of the largest epithermal gold deposits discovered to date.

Lihir Island is located at latitude 3°S, longitude 152°30′E, and has an area of about 192 km^2. The Ladolam gold deposit is located within the Luise crater on the east coast of Lihir Island and was discovered in 1982 by a Kennecott Explorations and Niugini Mining Joint Venture (Davies and Ballantyne, 1987; Moyle et al., 1990; Hoogvliet, 1993).

About 20% of the world's largest gold deposits are associated with shoshonitic and alkaline rocks, which are unlikely to exceed 3% by volume of subduction-related igneous rocks (Sillitoe, 1997; Müller and Groves, 2000). This observation even excludes those deposits associated with other potassic rock suites (e.g., high-K calc-alkaline rocks).

Previous work has shown that alkaline rocks associated with porphyry copper–gold and/or epithermal gold mineralization are characterized by high halogen concentrations, particularly Cl, and by high oxygen fugacities (Müller and Groves, 1993, 2000). The presence of sufficient halogens, such as Cl, is essen-

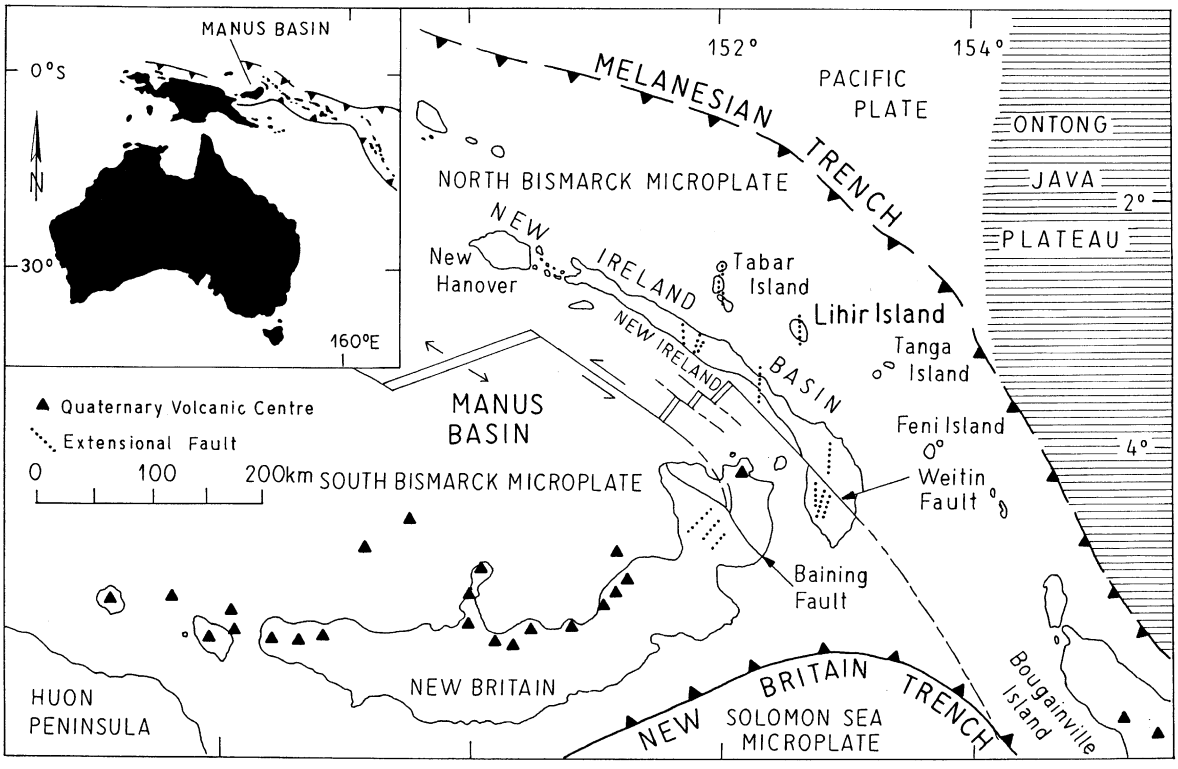

Fig. 1. Geographic overview of the location of Lihir Island and its tectonic setting. The Manus back-arc basin and the Melanesian and the New Britain trenches are shown. Black triangles mark the position of Quaternary volcanoes.

tial in controlling the abundances of Au and Cu in saline aqueous fluids that exsolve from a magma (Webster, 1992).

This study aims to document the geochemical characteristics of the alkaline host rocks of Lihir Island. While previous studies on other alkaline rock-hosted gold deposits could only indirectly infer their high oxygen fugacities, based on the presence of high primary magnetite contents and abundant sulphate phases, such as anhydrite veins (e.g., Müller and Groves, 2000), this is the first attempt to calculate the f_{O_2} of the host igneous rocks in relation to the FMQ buffer on the basis of olivine–spinel barometry (Ballhaus et al., 1991). The importance of a high f_{O_2} in the formation of hydrothermal ore deposits related to igneous intrusions will be discussed below.

2. Regional geology

The Bismarck archipelago is located northeast of the island of Papua New Guinea and includes the islands of New Britain, New Ireland, Bougainville and the Solomons (Fig. 1). Lihir Island is one of four volcanic island groups that form a chain parallel to the New Ireland coast line. The other islands are Tabar to the northwest and Tanga and Feni to the southeast (Davies and Ballantyne, 1987).

The plate tectonic situation in this area was formerly characterised by the southwestward subduction of the Pacific plate beneath the Melanesian arc (Fig. 1). Contemporaneous with this subduction process, calc-alkaline volcanism occurred during the Oligocene and Miocene on New Ireland. About 15 Ma ago, the southwestward subduction ceased due to the collision of the Ontong–Java Plateau with the Kilinailau trench (Coleman and Kroenke, 1981). This resulted in plate rotation and stress relocation. As a consequence, the northward movement of the Australian Plate generated the presently active north-dipping New Britain trench (Fig. 1). Related to this northward subduction, back-arc spreading processes developed in the Manus Basin separating the Bismarck microplate into northern and southern segments (Fig. 1). Partial melting of subduction-modified upper mantle sources beneath Lihir Island was probably triggered by adiabatic decompression melting along deep-seated extensional structures related to the back-arc rifting of the Manus Basin (e.g., Taylor, 1979; McInnes and Cameron, 1994).

The Tabar–Lihir–Tanga–Feni volcanic island chain extends for a distance of >260 km to the northeast of New Ireland. About 3.6 Ma, volcanic activity started on Simberi Island (Tabar island group) in the New Ireland fore-arc region (Rytuba et al., 1993). This high-K calc-alkaline volcanism seems to be related to lithospheric extension along northeast-trending faults, which were generated during the opening of the Manus back arc basin (Taylor, 1979; Steward and Sandy, 1988). The most recent on-land eruption is recorded on Feni Island about 2300 years ago (Licence et al., 1987).

Lihir Island consists of Pliocene–Pleistocene lavas, volcanic breccias, pyroclastic and epiclastic rocks derived from five volcanoes that dominate the island. These are, in chronological order, the Huniho, Wurtol, Luise, Londolovit and Kinami volcanoes (Fig. 2). While the Londolovit and Huniho volcanoes form the northern part of the island, the central part is dominated by the Wurtol and Luise volcanoes and the southern part by Kinami volcano. The Huniho crater is accompanied by numerous parasitic volcanoes on its northwestern flanks and probably represents the largest volcanic system on Lihir Island (Komyshan, 1999). Wallace et al. (1983) interpreted the Londolovit volcano as one of the largest and oldest on the island although its volcanic cone is not preserved. However, a modern photogeological study by Komyshan (1999) implies that Londolovit is probably only a small parasitic volcano of Huniho. The Wurtol volcano appears to overprint the volcanic products from Huniho, and its parasitic volcanoes are controlled by two north–northeast-trending structures (Komyshan, 1999). The Pleistocene Luise stratovolcano consists of an elongate elliptical crater whose northeastern margin has collapsed into the sea. The dimensions of this collapse amphitheatre are approximately 5.5 by 3.5 km and it hosts the giant Ladolam gold deposit. Extensive diamond drilling indicated that the Luise collapse amphitheatre does not represent a caldera, which has been suggested by several previous workers (e.g., Wallace et al., 1983; Moyle et al., 1990). However, it can rather be interpreted as a partial volcano slope failure (cf. Lopez and Williams, 1993; Voight and Elsworth, 1997) or

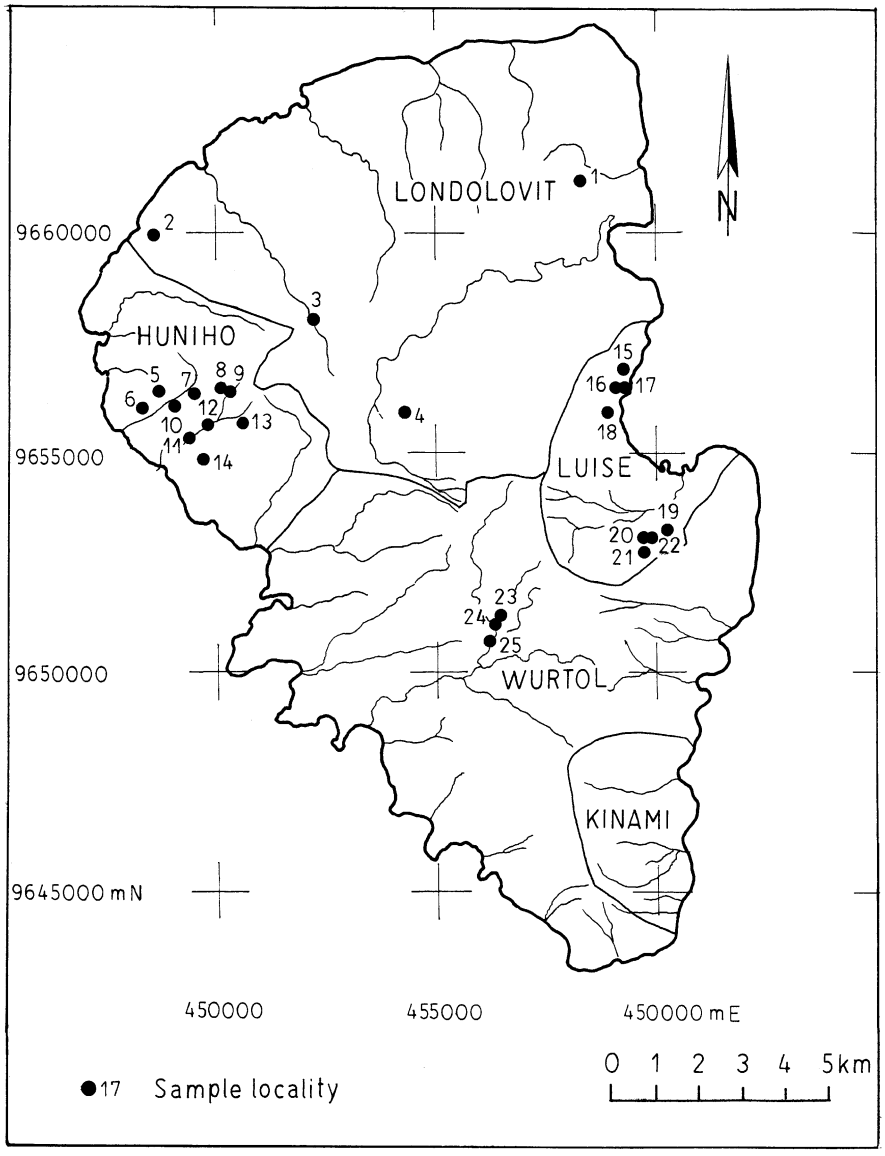

Fig. 2. Sample locality map of Lihir Island showing the five stratovolcanoes that dominate the island.

sector collapse of the original stratovolcano, possibly triggered by an earthquake, which has also been suggested by Sillitoe (1994). The lithostatic unloading during this process resulted in widespread hydraulic brecciation of the host rocks that was healed by anhydrite and calcite veining. The partial failure of the volcano slope also permitted the inflow of sea water into the open crater resulting in the formation of phreatomagmatic breccias that can be observed in the open pits of the Ladolam gold mine (Müller et al., 2001).

Ladolam is interpreted as an epithermal gold deposit (e.g., Moyle et al., 1990). Ongoing studies imply that in terms of gold mineralization, the process of lithostatic unloading due to the partial volcano slope failure, caused a switch from an original

porphyry gold mineralization style to an economically more important epithermal gold mineralization style (e.g., Müller et al., 2001 and references therein).

Based on the presence of two overlapping circular demagnetised zones in the magnetic data Luise volcano probably consisted of two eruptive centres (Komyshan, 1999). The southern centre hosts the Ladolam gold deposit, while the northern one is only partially exposed, with the majority now located beneath Luise Harbour. Development of the volcano resulted in deposition of interbedded pyroclastic rocks and lavas dipping at 20–30° away from the amphitheatre rim (Komyshan, 1999). Parasitic volcanoes have developed on the northwestern and southern margins of the main crater.

The youngest volcano on Lihir Island is Kinami, centered on a collapse crater in the southern part of the island. Similar to Luise volcano, the eastern portion of the original stratovolcano collapsed into the sea, probably also due to partial failure of the volcano slope. Parasitic volcanoes and cinder cones developed around the margin of the crater (Komyshan, 1999).

Hydrothermal alteration (argillic and phyllic) developed in most of the craters of the original and parasitic volcanoes as well as on fault zones. The location and geometry of this alteration is partially controlled by east–northeast-trending faults (Komyshan, 1999). Potassic alteration with hydrothermal biotite, was observed at Wurtol volcano to the southwest of Luise amphitheatre (i.e., samples 23, 25).

3. Structural setting

Based on a regional scale airphoto interpretation, the most prominent fractures on Lihir Island are shallowly dipping (40–50°) normal faults that generally dip away from the Luise and Kinami craters (Komyshan, 1999). The interpretation of magnetic data implies the presence of abundant north–south-trending faults on the island, which have only rarely been observed on airphotographs (Komyshan, 1999). However, these north–south-trending features may be correlated with the locally mapped Letomazien structures in the Minifie pit of the Ladolam gold mine (cf. Corbett, 1999).

On a mine scale, three major structural trends are evident. The most important feature in the upper part of the Minifie orebody is an east–northeast-trending and steeply north-dipping structural corridor up to 150 m wide, the Minifie fault zone, which largely controls the high-grade ore. On a regional scale, the east–northeast-trending structures appear to control the location of several hydrothermal alteration zones throughout the island. The second structural trend is represented by the north–south-oriented Letomazien structures and the third one comprises the west–northwest-trending Huniho structures (Corbett, 1999). The Letomazien structures are interpreted to represent the deep feeder zones of the epithermal gold-bearing fluids at Minifie. In the upper levels, the hydrothermal fluids diffused out of the Letomazien structures thus utilizing the highly permeable phreatomagmatic breccias as conduits. In contrast, the Huniho structures are mapped as an alignment of pyritic fluidized breccias and small shears (Corbett, 1999).

4. Mineralogy and petrography

Lihir Island consists of a suite of alkaline rocks ranging from porphyritic trachybasaltic, trachyandesitic and latitic lavas and pyroclastic rocks with high K_2O contents (Wallace et al., 1983), which, in some places, are cut by monzodiorite intrusions (see below). Several late-stage andesitic and latitic porphyry stocks and dykes have been intersected in drill holes (Moyle et al., 1990). More rarely, there are phonolites and olivine–clinopyroxene cumulates.

This study concentrates on samples from the Huniho, Londolovit, Wurtol and Luise volcanoes. The rocks from Londolovit are characterized by relatively primitive compositions, while those from Huniho range from relatively primitive to more evolved compositions. Only clinopyroxene cumulates, olivine basalts, trachybasalts and monzodiorites have been documented from Londolovit volcano. In contrast, rocks from Huniho volcano range from olivine–clinopyroxene cumulates through trachyandesites to latites that are cut by monzodiorite stocks. The rocks from Luise volcano comprise a series from rare leucite-bearing phonolites and olivine–clinopyroxene cumulates to trachyandesites and hypabyssal monzo-

diorite stocks. Volcanic rocks dominating the upper parts of the Ladolam gold deposit consist of lavas, tuffs, and volcanic breccias. They are porphyritic with phenocrysts of plagioclase, clinopyroxene, and minor phlogopite and amphibole in a feldspar-dominated groundmass. The pyroclastic rocks comprise lapilli and ash tuffs as well as phreatic and phreatomagmatic breccias that are well exposed in the two open pits at Lienetz and Minifie.

The samples collected for this study are mostly pristine and display primary igneous textures. However, two samples from Wurtol volcano (i.e., samples 23, 25) have been overprinted by moderate potassic alteration which led to the crystallization of hydrothermal biotite.

The volcanic and hypabyssal rocks of Lihir Island have porphyritic textures with a fine- to medium-grained groundmass. Only few samples display a very fine-grained or glassy groundmass as observed in trachybasalt sample 10, which additionally contains abundant vesicles suggestive of rapid uplift probably driven by high contents of volatile phases. Petrographically, the phonolite (i.e., sample 22) consists of leucite, clinopyroxene and amphibole phenocrysts in a fine-grained feldspar-dominated groundmass. The trachybasalts (e.g., samples 3, 10, 24) typically contain phenocrysts of amphibole, clinopyroxene and minor olivine, in a plagioclase-rich groundmass. The trachyandesites (e.g., samples 9, 13, 16) are characterized by phenocrysts of amphibole, clinopyroxene, and apatite microphenocrysts in a fine-grained feldspar-bearing groundmass. The latites (e.g., samples 8, 11) are characterized by phenocrysts of phlogopite, clinopyroxene and amphibole in a fine-grained feldspar-dominated groundmass.

The plutonic rocks collected from Lihir Island consist of medium-grained monzodiorite (e.g., samples 4, 5, 17, 23) comprising phlogopite, brown and/or green amphibole, clinopyroxene and plagioclase, with minor olivine, alkali feldspar and apatite. The rocks normally have massive equigranular textures, but plagioclase may form relatively large crystals (up to 2 mm). The monzodiorites commonly contain xenoliths of clinopyroxene and magnetite (e.g., samples 15, 17).

The mineral chemistry of olivines, clinopyroxenes, amphiboles and spinels has been determined using a JEOL JXA8900 electron microprobe with five spectrometers and WDS attachment at TU Bergakademie Freiberg. Major and minor elements were determined at 15 kV acceleration voltage and a beam current of 20 nA, with counting times of 20 s for Si, Al, Mg, Ca, Sr, Ba and K, and 30 s for Fe, Ni, Na, Cr, Mn and Ti. The standard sets of the Smithsonian Institute (cf. Jarosewich et al., 1980) and JEOL were used for reference. Representative mineral analyses of amphiboles, clinopyroxenes, spinels, olivines and micas are shown in Tables 1–5. The entire dataset is available from the first author on request.

Olivine, which often shows limonitic coating along the margin and on cracks, is restricted to the more primitive samples such as cumulates (i.e., samples 1 and 19), olivine basalts (i.e., samples 2 and 6) and mafic monzodiorites (i.e., samples 4 and 15). Euhedral olivine phenocrysts yield a forsterite content of 65–75 mol% and relatively high CaO contents of up to 0.48 wt.%. Xenomorphic olivine xenocrysts are easily distinguished from the phenocrysts by their elevated forsterite contents, 90–91 mol%, and by higher Ni contents (Table 1). They commonly show inclusions of chromian spinel and also display elevated CaO contents of more than 0.3 wt.%.

Clinopyroxene forms pale green, short prismatic crystals in the volcanics and hypabyssal intrusions and can be classified as diopside and augite (classification of Morimoto et al., 1988). These crystals reveal compositional variability between samples with $Wo_{39.2-46.7}En_{41.5-55.1}Fs_{1.5-12.4}$ (Table 2). Hypidiomorphic clinopyroxene crystals and aggregates in the cumulates are augite ($Wo_{36.7-41.6}En_{46.4-58.2}Fs_{4.1-12.0}$), which yields the highest Al_2O_3 and TiO_2 contents (up to 7.4 and 1.1 wt.%, respectively). All clinopyroxene crystals reveal distinct zoning with increasing TiO_2 and CaO contents, at the expense of MgO, from core to rim. Most of the investigated clinopyroxene crystals yield elevated ferric iron, with an average content of 65% Fe_2O_3 of total iron. This is in accord with the observations of earlier studies on alkaline rocks from Luise volcano (see Kennedy et al., 1990). The alkaline rocks from Lihir Island generally lack orthopyroxene.

Amphibole phenocrysts consist of brown to olive-green subtypes. The brown amphibole phenocrysts are normally completely replaced by fine-

Table 1
Representative analyses of olivine phenocrysts (PC) and xenocrysts (XC). For abbreviation of rock types, see Table 5

Sample	6	6	3	3	19	19	1	1	4	4
Rock type	OB	OB	TB	TB	C	C	C	C	MD	MD
Wt.%	XC1	XC2	PC1	PC2	PC1	PC2	PC1	PC2	PC1	PC2
SiO_2	39.66	39.87	37.11	37.37	38.87	39.17	37.52	37.62	38.19	38.42
TiO_2	0.01	0.03	0.00	0.02	0.03	0.00	0.03	0.00	0.03	0.00
Al_2O_3	0.02	0.01	0.01	0.02	0.03	0.04	0.03	0.03	0.02	0.01
Cr_2O_3	0.02	0.01	0.01	0.01	0.02	0.00	0.00	0.02	0.00	0.01
MgO	49.52	49.32	31.79	31.82	38.59	40.66	33.19	32.85	36.58	37.10
CaO	0.32	0.32	0.38	0.37	0.36	0.37	0.39	0.37	0.22	0.22
MnO	0.17	0.18	0.90	0.99	0.56	0.53	0.96	0.95	0.70	0.74
FeO	8.85	8.75	30.67	30.61	22.43	20.52	29.22	29.46	25.15	24.45
NiO	0.10	0.15	0.00	0.01	0.02	0.07	0.01	0.05	0.03	0.01
Total	98.67	98.63	100.86	101.22	100.91	101.37	101.35	101.35	100.93	100.96
Cations (O = 4)										
Si	0.984	0.989	1.000	1.003	1.003	0.997	0.999	1.002	0.999	1.001
Ti	0.000	0.000	0.000	0.000	0.001	0.000	0.001	0.000	0.001	0.000
Al	0.001	0.000	0.000	0.001	0.001	0.001	0.001	0.001	0.001	0.000
Cr	0.000	0.000	0.000	0.000	0.000	0.000	0.000	0.000	0.000	0.000
Mg	1.832	1.824	1.277	1.273	1.485	1.543	1.317	1.304	1.427	1.441
Ca	0.009	0.008	0.011	0.011	0.010	0.010	0.011	0.011	0.006	0.006
Mn	0.004	0.004	0.021	0.022	0.012	0.011	0.022	0.021	0.015	0.016
Fe	0.184	0.182	0.691	0.687	0.484	0.437	0.650	0.656	0.550	0.533
Ni	0.002	0.003	0.000	0.000	0.000	0.002	0.000	0.001	0.001	0.000
Total	3.015	3.010	3.000	2.996	2.996	3.002	3.000	2.997	3.000	2.999
Endmembers										
Mg_2SiO_4	90.25	90.26	63.86	63.87	74.55	77.04	65.83	65.43	71.36	72.17
Fe_2SiO_4	9.05	8.99	34.56	34.46	24.30	21.81	32.52	32.91	27.52	26.68
Ca_2SiO_4	0.42	0.42	0.55	0.53	0.50	0.50	0.56	0.53	0.31	0.31
Ni_2SiO_4	0.10	0.15	0.00	0.01	0.02	0.07	0.01	0.06	0.04	0.01
Mn_2SiO_4	0.18	0.18	1.03	1.12	0.62	0.57	1.08	1.07	0.77	0.82

Table 2
Representative analyses of clinopyroxene with an endmember calculation after Lindsley (1983). The pressure estimate using the calibration of (Nimis, 1995; cf. P_N in the last line) is affected by an error of ± 2 kbar. Note the low and even negative pressures calculated with this calibration.

Sample	22	13	18	18	20	12	2	1	1	19	19	4	4	3	3	6	6
Rock type	Ph	TA	MD	MD	TA	TA	OB	C	C	C	C	MD	MD	TB	TB	OB	OB
Wt.%	Cpx core	Cpx core	Cpx core	Cpx rim	Cpx core	Cpx core	Cpx core	Cpx core	Cpx rim	Cpx core	Cpx rim	Cpx core	Cpx rim	Cpx core	Cpx rim	Cpx core	Cpx rim
SiO_2	51.64	50.37	51.46	51.39	49.86	49.01	53.50	51.50	47.18	47.50	46.81	49.42	48.33	51.48	49.26	53.74	50.30
TiO_2	0.48	0.54	0.36	0.58	0.72	0.88	0.19	0.38	0.81	0.68	1.13	0.59	0.81	0.55	0.90	0.19	0.64
Al_2O_3	2.70	4.23	3.21	2.54	3.73	5.53	1.47	3.14	5.91	6.48	7.38	4.15	5.24	2.95	4.75	1.14	3.71
Cr_2O_3	0.00	0.01	0.20	0.00	0.03	0.00	0.20	0.07	0.00	0.00	0.01	0.01	0.04	0.03	0.02	0.45	0.07
Fe_2O_3	3.33	4.03	2.31	2.70	4.98	4.23	1.92	3.86	7.17	5.48	5.53	4.30	5.14	1.87	3.52	1.19	4.37
MgO	12.89	13.47	15.53	13.92	13.72	12.61	17.27	15.49	13.42	13.01	12.36	14.54	14.00	14.50	13.37	17.56	15.43
CaO	23.32	22.97	22.82	22.54	22.78	23.08	24.13	23.04	22.72	22.35	22.44	22.75	23.03	21.90	22.20	24.14	23.08
MnO	0.56	0.39	0.10	0.52	0.30	0.29	0.05	0.13	0.17	0.19	0.16	0.14	0.16	0.32	0.25	0.07	0.09
FeO	5.30	4.45	3.71	5.34	3.42	4.49	1.58	3.17	1.62	3.40	4.07	3.02	2.61	6.10	5.36	1.30	1.61
Na_2O	0.75	0.52	0.24	0.52	0.63	0.55	0.17	0.31	0.49	0.43	0.43	0.29	0.27	0.37	0.39	0.18	0.41
K_2O	0.00	0.01	0.01	0.00	0.00	0.01	0.01	0.00	0.02	0.00	0.00	0.01	0.01	0.00	0.00	0.00	0.01
Total	100.96	100.98	99.94	100.07	100.17	100.66	100.47	101.09	99.51	99.52	100.31	99.22	99.62	100.06	100.02	99.97	99.71
Cations (O = 6)																	
Si	1.908	1.856	1.894	1.909	1.851	1.816	1.941	1.879	1.764	1.776	1.744	1.843	1.800	1.907	1.835	1.954	1.855
Ti	0.013	0.015	0.010	0.016	0.020	0.024	0.005	0.010	0.023	0.019	0.032	0.017	0.023	0.015	0.025	0.005	0.018
Al	0.118	0.184	0.139	0.111	0.163	0.241	0.063	0.135	0.260	0.286	0.324	0.182	0.230	0.129	0.209	0.049	0.161
Fe^{3+}	0.093	0.112	0.064	0.076	0.139	0.118	0.052	0.106	0.202	0.154	0.155	0.121	0.144	0.052	0.099	0.033	0.121
Cr	0.000	0.000	0.006	0.000	0.001	0.000	0.006	0.002	0.000	0.000	0.000	0.000	0.001	0.001	0.001	0.013	0.002
Mg	0.710	0.740	0.852	0.771	0.759	0.696	0.934	0.843	0.748	0.725	0.686	0.808	0.777	0.801	0.743	0.952	0.848
Ca	0.923	0.907	0.900	0.897	0.906	0.916	0.938	0.901	0.910	0.896	0.896	0.909	0.919	0.869	0.886	0.940	0.912
Fe^{2+}	0.164	0.137	0.114	0.166	0.106	0.139	0.048	0.097	0.051	0.106	0.127	0.094	0.081	0.189	0.167	0.040	0.050
Mn	0.018	0.012	0.003	0.016	0.009	0.009	0.002	0.004	0.005	0.006	0.005	0.004	0.005	0.010	0.008	0.002	0.003
Na	0.053	0.037	0.017	0.037	0.045	0.039	0.012	0.022	0.035	0.031	0.031	0.021	0.020	0.027	0.028	0.013	0.030
K	0.000	0.000	0.000	0.000	0.000	0.001	0.000	0.000	0.001	0.000	0.000	0.001	0.000	0.000	0.000	0.000	0.000
Total	4.000	4.000	4.000	4.000	4.000	4.000	4.000	4.000	4.000	4.000	4.000	4.000	4.000	4.000	4.000	4.000	4.000
Endmembers after Lindsley (1983)																	
Wo	0.456	0.415	0.416	0.438	0.421	0.410	0.450	0.412	0.378	0.371	0.367	0.403	0.392	0.417	0.400	0.459	0.416
En	0.442	0.493	0.515	0.463	0.508	0.491	0.523	0.527	0.582	0.549	0.534	0.534	0.550	0.472	0.490	0.520	0.551
Fs	0.102	0.092	0.069	0.099	0.071	0.099	0.027	0.061	0.041	0.081	0.099	0.063	0.058	0.111	0.110	0.022	0.033
P_N (kbar)	−2.7	−0.7	−0.5	−2.7	−1.4	0.5	−1.4	−1.0	1.4	1.7	1.6	−0.4	0.1	−1.7	−0.8	−1.3	0.3

Table 3
Representative analyses of clinoamphibole as well as primary and secondary mica. $P_{A\&S}$ is the Al-in-hornblende barometry of Anderson and Smith (1995), which has a systematic error of ± 1 kbar and T_C is the Ti in hornblende barometry after Colomby (1988). For rock abbreviations, see Table 5

Sample	20	20	9	9	12	Sample	15	26	26	25	17	27
Rock type	TA	TA	TA	TA	TA	Rock type	MD	TB	TB	TA	MD	A TB
Wt.%	Hbl	Hbl	Hbl	Hbl	Hbl	Wt.%	Phl	Phl	Phl	Bt	Phl	Bt
SiO_2	39.58	39.84	41.83	41.78	39.77	SiO_2	40.55	40.06	40.34	36.40	40.69	36.02
TiO_2	3.02	2.99	2.93	2.99	2.40	TiO_2	2.49	2.32	2.28	4.34	2.71	3.68
Al_2O_3	11.83	11.95	12.38	12.64	13.16	Al_2O_3	13.12	11.96	11.71	14.15	11.43	16.17
Fe_2O_3	3.01	2.72	2.71	2.45	3.23	Cr_2O_3	0.01	0.03	0.00	0.00	0.02	0.00
Cr_2O_3	0.00	0.00	0.02	0.00	0.03	MgO	21.36	21.50	21.89	12.34	21.34	16.90
MgO	12.93	12.82	13.67	13.60	12.05	CaO	0.01	0.03	0.02	0.03	0.00	0.02
CaO	11.94	11.93	11.88	11.92	11.98	MnO	0.12	0.13	0.14	0.39	0.16	0.19
MnO	0.26	0.29	0.28	0.29	0.28	FeO	6.42	7.43	7.77	17.79	7.02	11.23
FeO	10.18	10.42	9.16	9.38	10.92	BaO	0.00	0.00	0.00	0.00	0.00	0.00
Na_2O	2.60	2.59	2.55	2.59	2.59	Na_2O	0.85	0.88	0.97	0.33	1.00	0.74
K_2O	1.41	1.45	1.33	1.31	1.38	K_2O	9.11	9.42	9.56	9.91	9.62	9.67
Total	96.76	96.99	98.74	98.94	97.78	H_2O-	1.90	1.78	1.63	3.91	1.54	3.86
Cations (O = 23)						F-	4.70	4.85	5.22	0.00	5.39	0.31
Si	5.980	6.003	6.114	6.096	5.953	Cl-	0.06	0.05	0.06	0.12	0.06	0.08
Ti	0.343	0.339	0.322	0.328	0.270	Total	98.71	98.38	99.38	99.69	98.69	98.72
Al	2.106	2.122	2.133	2.173	2.322	Cations (O = 12)						
Fe^{3+}	0.342	0.308	0.298	0.268	0.363	Si	2.934	2.937	2.936	2.769	2.972	2.680
Cr	0.000	0.000	0.002	0.000	0.004	Ti	0.136	0.128	0.125	0.248	0.149	0.206
Mg	2.912	2.879	2.979	2.958	2.689	Al	1.119	1.033	1.005	1.268	0.984	1.418
Ca	1.933	1.926	1.860	1.863	1.921	Cr	0.001	0.002	0.000	0.000	0.001	0.000
Mn	0.033	0.037	0.035	0.036	0.036	Mg	2.304	2.350	2.375	1.399	2.323	1.875
Fe^{2+}	1.287	1.312	1.120	1.144	1.367	Ca	0.001	0.002	0.002	0.002	0.000	0.002
Na	0.762	0.757	0.723	0.733	0.752	Mn	0.007	0.008	0.009	0.025	0.010	0.012
K	0.272	0.279	0.248	0.244	0.264	Fe	0.389	0.455	0.473	1.132	0.429	0.699
Total	15.970	15.961	15.833	15.844	15.940	Ba	0.000	0.000	0.000	0.000	0.000	0.000
T_C (°C)	936	932	916	922	865	Na	0.119	0.125	0.137	0.049	0.142	0.107
$P_{A\&S}$ (kbar)	−0.2	−0.1	−0.1	0.1	0.5	K	0.841	0.881	0.888	0.962	0.896	0.918
						Total	7.851	7.921	7.949	7.854	7.906	7.917
						OH	0.917	0.869	0.791	1.985	0.748	1.917
						F	1.076	1.124	1.202	0.000	1.245	0.073
						Cl	0.007	0.006	0.007	0.015	0.007	0.010
						X_{Mg}	0.856	0.838	0.834	0.553	0.844	0.728

grained aggregates of leucoxene, with their remnants rarely preserved in the cores. In contrast, green amphibole phenocrysts are generally fresh. Both types can be classified as Mg-hastingsite following the classification of Leake et al. (1997), with the brown amphibole containing slightly higher TiO_2 contents (about 3 wt.%) than the green (about 2.5 wt.%; cf. Table 3).

There is a clear distinction between two generations of *mica* (Table 3). Primary (magmatic) mica can be classified as Mg-rich phlogopite and commonly occurs in latites and monzodiorites (e.g., samples 8, 11, 15, 17) while secondary (hydrothermal) mica is Fe-rich biotite generated during potassic alteration in the vicinity of the porphyry Au–Cu mineralization that predates subsequent epithermal-style gold mineralization at Ladolam. This is in contrast to the observation that hydrothermal mica is usually characterized by higher Mg contents than its magmatic precursor (cf. Beane and Titley, 1981). The differences between magmatic and hydrothermal mica are shown on the molecular Al–Fe–Mg triangular plot (Fig. 3). Magmatic phlogopite contains very high F contents (up to 5.22 wt.%), and distinctly lower Cl concentrations (< 0.08 wt.%). In contrast, hydrothermal biotite has high Cl concentrations (up to 0.15 wt.%) and very low F contents

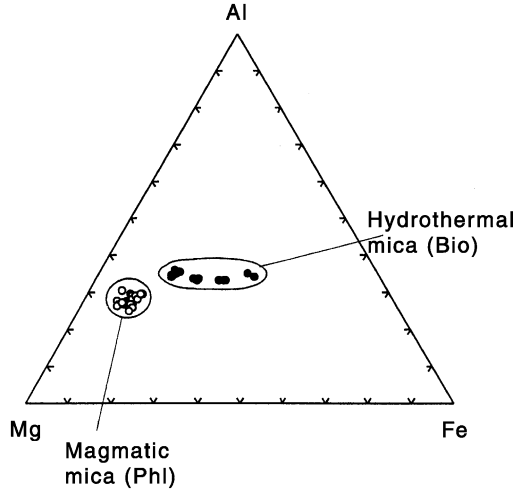

Fig. 3. Al–Mg–Fe triangular plot showing the compositions of mica phenocrysts from Lihir Island. Open circles are primary (magmatic) phlogopites and black dots are secondary (hydrothermal) biotites.

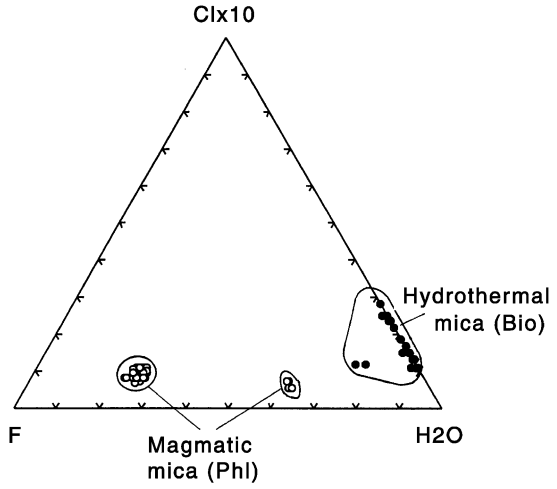

Fig. 4. $Cl \times 10–F–H_2O$ triangular plot showing the volatile contents of mica phenocrysts from Lihir Island. Open circles are primary (magmatic) phlogopites and black dots are secondary (hydrothermal) biotites.

(< 0.08 wt.%), as shown on the $Cl–F–H_2O$ triangular plot (Fig. 4).

Spinel in most samples is titanomagnetite with up to 9 wt.% TiO_2. Uncommonly, dark brown chromian spinel with X_{Cr} ($= Cr/(Cr + Al)$) values of 0.73–0.75 is observed beside titanomagnetite (cf. sample 6 in Table 4). The chromian spinel octahedra typically form inclusions in olivine (Fo_{90-91}) and are interpreted as mantle xenocrysts.

5. Geochemistry

Whole-rock major element analyses of 25 regional samples from Lihir Island were performed at ACME Analytical Laboratories in Vancouver, Canada, using XRF facilities. The sample localities are shown in Fig. 2. The trace and rare earth elements have been assayed with ICP-MS at ACME Laboratories, Vancouver, and both the data and detection limits are shown in Table 5. Geochemically, the alkaline rocks from Lihir Island range from primitive to relatively evolved compositions, as reflected by SiO_2 (45.77–54.97 wt.%), MgO (1.40–15.30 wt.%) contents and variable concentrations of the mantle-compatible elements (130–328 ppm V, 1–186 ppm Ni). These data are consistent with the

Table 4
Representative analyses of chromian spinel xenocrysts (CrSpl) and Ti-magnetite phenocrysts (TiMag) with results of the Spl-Ol geothermometry (T_{BBG}) of Ballhaus et al. (1991). The $\Delta \log f_{O_2}$ values were calculated with the QUILF program (cf. samples 3,19,1,4) and after Ballhaus et al. (1991; cf. sample 6)

Sample	6	6	6	3	3	19	19	1	1	4	4
Rock type	OB	OB	OB	TB	TB	C	C	C	C	MD	MD
Wt.%	CrSpl	CrSpl	CrSpl	TiMag	TiMag	TiMag	TiMag	TiMag	TiMag	TiMag	TiMag
SiO_2	0.06	0.03	0.04	0.16	0.20	0.12	0.14	0.05	0.07	0.15	0.09
TiO_2	0.66	0.60	0.60	9.23	9.09	6.18	6.25	7.46	7.79	6.37	8.31
Al_2O_3	11.56	10.76	12.12	4.23	4.81	7.82	7.72	2.85	4.14	6.76	5.01
Cr_2O_3	49.39	49.36	48.99	0.05	0.01	0.62	0.61	0.30	0.39	0.02	0.06
Fe_2O_3	9.89	10.74	9.45	46.17	45.62	47.94	48.04	51.17	48.77	49.13	48.15
MgO	11.82	11.54	11.82	2.22	2.75	2.74	2.59	1.54	1.86	2.97	2.89
CaO	0.05	0.03	0.07	0.03	0.03	0.00	0.00	0.06	0.01	0.02	0.05
MnO	0.14	0.15	0.14	0.64	0.60	0.45	0.45	0.65	0.57	0.60	0.61
FeO	15.98	16.07	15.74	36.10	35.18	33.39	33.84	35.22	35.28	32.77	34.55
NiO	0.02	0.07	0.09	0.02	0.02	0.05	0.01	0.01	0.04	0.00	0.00
Total	99.56	99.35	99.05	98.85	98.31	99.31	99.65	99.31	98.92	98.79	99.72
Cations (O = 3)											
Si	0.002	0.001	0.001	0.006	0.007	0.004	0.005	0.002	0.003	0.005	0.003
Ti	0.016	0.015	0.015	0.257	0.253	0.168	0.170	0.210	0.218	0.175	0.228
Al	0.445	0.417	0.467	0.185	0.210	0.333	0.328	0.126	0.182	0.291	0.215
Cr	1.276	1.285	1.268	0.001	0.000	0.018	0.017	0.009	0.011	0.001	0.002
Fe^{3+}	0.243	0.266	0.233	1.287	1.270	1.304	1.305	1.442	1.366	1.348	1.321
Mg	0.576	0.566	0.577	0.123	0.152	0.148	0.139	0.086	0.103	0.161	0.157
Ca	0.002	0.001	0.002	0.001	0.001	0.000	0.000	0.002	0.000	0.001	0.002
Mn	0.004	0.004	0.004	0.020	0.019	0.014	0.014	0.021	0.018	0.019	0.019
Fe^{2+}	0.436	0.442	0.431	1.119	1.088	1.010	1.021	1.103	1.098	0.999	1.053
Ni	0.001	0.002	0.002	0.001	0.001	0.001	0.000	0.000	0.001	0.000	0.000
Total	3.000	3.000	3.000	3.000	3.000	3.000	3.000	3.000	3.000	3.000	3.000
X_{Mg}	0.57	0.56	0.57	0.10	0.12	0.13	0.12	0.07	0.09	0.14	0.13
X_{Cr}	0.74	0.75	0.73	0.01	0.00	0.05	0.05	0.07	0.06	0.00	0.01
T_{BBG} (°C)	924	927	920	893	965	805	787	802	832	894	903
$\Delta \log f_{O_2}$	2.12	2.27	2.04	3.67	3.56	4.09	4.11	3.89	3.80	3.89	3.94

Table 5
Major element (wt.%) and trace element (ppm) composition of the magmatic rocks from Lihir island. Rock abbreviations are: C = cumulate; OB = olivine basalt; TB = trachybasalt; A TB = strongly altered trachybasalt; MD = monzodiorite; L = latite; TA = trachyandesite; Ph = phonolite

Sample	1	2	3	4	5	6	7	8	9	10	11	12	
Volcano	Londolovit	Huniho	Londolovit	Londolovit	Huniho	Huniho	Huniho	Huniho	Huniho	Huniho	Huniho	Huniho	
Rock type	C	C	TB	MD	MD	C	MD	L	TA	TB	L	TA	Detection limit
SiO_2	48.33	48.59	48.73	51.12	49.08	45.77	49.57	51.30	52.01	48.76	54.97	51.24	0.02%
TiO_2	0.72	0.59	1.08	1.01	1.10	0.62	1.07	0.97	0.94	1.11	0.75	0.87	0.01%
Al_2O_3	9.29	7.84	16.43	17.08	17.67	6.72	16.48	17.12	18.43	15.91	19.27	16.79	0.03%
Fe_2O_3 (total)	10.58	8.62	11.66	10.51	10.32	9.46	9.90	9.20	9.12	10.39	6.61	9.13	0.04%
MnO	0.20	0.17	0.22	0.20	0.21	0.19	0.18	0.22	0.22	0.16	0.12	0.21	0.01%
MgO	11.13	12.76	5.20	4.55	3.94	15.30	4.23	3.90	3.17	4.45	2.36	3.13	0.01%
CaO	15.45	17.67	10.17	8.93	9.05	16.22	9.73	8.05	7.27	8.91	5.97	6.53	0.01%
Na_2O	1.72	1.28	2.70	3.02	3.37	0.71	3.76	3.96	3.84	2.56	4.49	3.16	0.01%
K_2O	0.86	0.29	1.97	2.75	1.47	0.45	1.88	2.10	3.50	3.20	3.83	4.68	0.04%
P_2O_5	0.36	0.26	0.32	0.36	0.43	0.22	0.35	0.42	0.42	0.43	0.28	0.46	0.01%
LOI	1.20	2.00	1.20	1.00	3.40	4.50	3.10	2.80	1.60	3.00	2.00	2.70	0.10%
Total	100.04	100.23	99.84	100.70	100.23	100.39	100.42	100.24	100.69	99.05	100.82	99.13	
ne%	0	0	0	0	0	0	0.69	0	0	0	0	0	
mg#	71	77	51	50	47	79	50	50	45	50	45	44	
V	236	190	321	224	296	191	222	200	246	327	141	231	5 ppm
Co	44	42	36	29	26	50	27	23	23	30	43	24	0.5 ppm
Ni	32	22	9	10	4	42	8	38	3	9	4	4	1 ppm
Cu	105	81	132	135	99	61	131	105	124	161	37	124	1 ppm
Zn	56	41	80	61	50	42	69	38	24	95	44	117	1 ppm
Rb	79	186	25	48	19	17	40	51	56	47	72	79	0.5 ppm
Sr	920	731	1020	969	1107	664	1116	1244	1021	1002	959	1465	0.5 ppm
Y	16	12	21	27	25	10	26	30	22	28	27	27	0.1 ppm
Zr	46	37	58	76	87	30	87	111	74	81	89	117	0.5 ppm

Nb	1.2	1.4	1.5	2	3.3	1.2	3.3	4.2	2.4	2.8	2	4.2	0.5 ppm
Ba	124	95	218	291	278	108	270	377	270	236	330	366	0.5 ppm
La	9.4	8.0	10.8	14.9	15.0	6.7	14.2	16.7	15.5	15.5	14.1	20.3	0.5 ppm
Ce	21.1	16.6	23.0	28.9	29.7	15.0	30.0	35.0	30.7	31.5	24.2	38.4	0.5 ppm
Nd	15.1	11.9	16.4	18.6	20.1	11.0	19.2	21.1	18.8	21.5	17.6	22.2	0.4 ppm
Sm	4.1	3.2	4.2	4.6	5.0	2.8	4.9	5.1	4.4	5.6	4.4	5.4	0.1 ppm
Eu	1.3	1.1	1.5	1.6	1.7	0.9	1.6	1.7	1.5	1.8	1.4	1.8	0.05 ppm
Tb	0.56	0.43	0.62	0.76	0.78	0.37	0.77	0.85	0.69	0.84	0.69	0.84	0.01 ppm
Dy	3.10	2.46	3.84	4.31	4.48	2.18	4.67	5.00	3.98	5.02	4.22	4.89	0.05 ppm
Ho	0.59	0.44	0.80	0.91	0.91	0.37	0.96	1.07	0.80	1.01	0.86	0.96	0.05 ppm
Er	1.54	1.02	2.20	2.48	2.57	0.93	2.66	3.04	2.21	2.84	2.36	2.83	0.05 ppm
Tm	0.23	0.18	0.34	0.42	0.39	0.14	0.41	0.50	0.36	0.43	0.39	0.44	0.05 ppm
Yb	1.16	0.90	1.66	2.30	2.25	0.70	2.42	2.85	2.11	2.60	2.16	2.52	0.05 ppm
Lu	0.19	0.16	0.27	0.33	0.36	0.12	0.36	0.45	0.31	0.39	0.31	0.39	0.01 ppm
Hf	1.4	1.1	1.7	2.0	2.3	1.1	2.5	3.0	2.0	2.3	2.5	2.8	0.5 ppm
Ta	0.1	0.1	0.1	0.1	0.1	0.1	0.2	0.2	0.1	0.1	0.1	0.2	0.1 ppm
Th	0.8	0.7	0.9	1.4	1.3	0.7	1.7	1.8	1.7	1.4	1.7	2.3	0.1 ppm
U	0.5	0.4	0.5	0.6	1.0	0.4	1.1	1.2	1.1	1.1	1.1	1.6	0.1 ppm
K_2O/Na_2O	0.5	0.2	0.7	0.9	0.4	0.6	0.5	0.5	0.9	1.2	0.9	1.5	
Ce/Yb	18.2	18.4	13.9	12.6	13.2	21.4	12.4	12.3	14.6	12.1	11.2	15.2	
Ta/Yb	0.09	0.11	0.06	0.04	0.04	0.14	0.08	0.07	0.05	0.04	0.05	0.08	
Ba/La	13.2	11.8	20.1	19.5	18.5	16.1	19	22.6	17.4	15.2	23.4	18	
U/Th	0.62	0.57	0.55	0.43	0.77	0.57	0.65	0.66	0.65	0.78	0.65	0.69	

(continued on next page)

Table 5 (*continued*)

Sample	13	14	15	16	17	18	19	20	21	22	23	24	25
Volcano	Huniho	Huniho	Luise	Luise	Luise	Luise	Luise	Luise	Luise	Luise	Wurtol	Wurtol	Wurtol
Rock type	TA	TB	MD	TA	MD	MD	C	TA	TB	Ph	MD	TB	TA
SiO_2	51.51	48.51	51.78	49.70	51.50	52.86	49.71	52.39	46.80	52.11	53.21	49.91	50.16
TiO_2	0.90	1.08	0.89	0.94	0.92	0.87	0.89	0.92	0.99	0.68	0.86	0.95	0.87
Al_2O_3	17.41	15.56	17.01	20.77	17.05	16.97	12.88	18.70	13.92	18.60	18.40	16.63	16.73
Fe_2O_3 (total)	9.40	11.33	9.13	6.98	9.75	9.00	11.51	8.74	12.40	6.61	7.26	10.58	9.03
MnO	0.22	0.21	0.20	0.13	0.21	0.20	0.22	0.21	0.21	0.19	0.08	0.29	0.20
MgO	3.06	5.65	3.58	1.40	3.78	3.84	7.33	2.42	6.07	2.50	3.29	4.88	3.87
CaO	8.81	11.14	8.36	3.07	7.40	8.05	11.83	7.01	12.23	7.02	0.98	9.57	5.87
Na_2O	3.78	2.66	3.60	3.65	3.22	3.69	2.63	3.64	2.43	4.58	5.97	3.01	3.14
K_2O	2.56	1.87	3.26	3.77	3.09	3.28	1.63	3.68	1.43	4.47	4.33	2.52	5.11
P_2O_5	0.40	0.39	0.37	0.49	0.39	0.34	0.47	0.38	0.53	0.33	0.34	0.35	0.44
LOI	1.40	1.40	2.50	8.30	2.60	1.40	1.40	2.20	2.90	1.80	4.10	1.20	3.50
Total	99.62	99.98	100.84	99.37	100.05	100.66	100.73	100.48	100.12	99.14	98.96	100.07	99.11
ne%	0	0	0	0	0	0	0	0	0	7.53	3.47	0	1.7
mg#	43	54	48	31	47	50	60	39	53	47	51	52	50
V	130	328	187	163	209	211	228	160	274	241	218	280	255
Co	23	33	25	28	26	24	43	23	41	17	22	32	19
Ni	35	11	7	186	8	7	17	2	11	1	40	12	11
Cu	50	150	80	148	141	92	292	84	196	145	43	185	142
Zn	35	79	68	186	75	69	73	49	80	72	40	64	60
Rb	49	60	57	69	57	57	58	40	101	45	87	41	57
Sr	1067	1022	976	770	774	910	1386	1168	1316	1461	743	1137	1146
Y	29	23	25	31	31	24	20	36	21	19	20	22	23
Zr	72	68	82	132	79	81	64	95	62	81	80	64	72

Nb	2	2.4	1.9	2.9	2	1.9	1.6	2.6	1.8	3	2.2	1.5	1.9
Ba	250	278	263	505	322	274	237	353	253	760	323	273	486
La	16.6	11.1	12.2	17.1	14.3	11.8	12.4	16.3	14.8	16.2	17.1	10.2	13.5
Ce	29.6	22.3	25.9	38.3	27.4	25.0	27.3	33.0	32.0	32.0	32.8	23.0	27.9
Nd	21.0	15.7	17.0	26.6	20.1	16.1	19.0	23.2	21.6	18.8	19.2	16.6	19.0
Sm	4.7	4.3	4.3	6.6	5.1	4.7	4.6	5.4	5.4	4.2	4.5	4.3	4.4
Eu	1.7	1.4	1.4	2.1	1.7	1.5	1.6	1.9	1.8	1.3	1.5	1.5	1.5
Tb	0.77	0.71	0.70	0.91	0.83	0.69	0.64	0.94	0.71	0.62	0.62	0.67	0.73
Dy	4.56	4.19	4.34	5.51	4.93	4.17	3.84	5.74	3.91	3.32	3.60	4.17	4.12
Ho	1.01	0.84	0.86	1.12	0.98	0.88	0.73	1.18	0.77	0.68	0.73	0.81	0.87
Er	2.73	2.37	2.44	3.21	2.79	2.45	1.96	3.38	1.95	1.88	1.95	2.34	2.37
Tm	0.43	0.35	0.42	0.51	0.47	0.38	0.31	0.53	0.31	0.33	0.34	0.33	0.37
Yb	2.54	2.00	2.17	2.80	2.56	2.28	1.68	2.91	1.70	1.65	1.92	1.94	2.19
Lu	0.36	0.30	0.34	0.41	0.37	0.35	0.26	0.45	0.25	0.28	0.32	0.28	0.33
Hf	2.0	1.8	2.3	3.7	2.3	2.2	1.8	2.6	1.9	2.1	2.3	1.8	2.0
Ta	0.1	0.1	0.1	0.1	0.1	0.1	0.1	0.1	0.1	0.2	0.1	0.1	0.1
Th	1.3	1.0	1.3	2.0	1.3	1.2	1.1	1.8	1.3	2.2	1.7	0.8	1.3
U	0.4	0.7	0.9	1.5	0.9	0.9	0.7	0.6	0.9	1.6	1.3	0.7	0.9
K_2O/Na_2O	0.7	0.7	0.9	1.0	1.0	0.9	0.6	1.0	0.6	1.0	0.7	0.8	1.6
Ce/Yb	11.6	11.1	11.9	13.7	10.7	11	16.2	11.3	18.8	19.4	17.1	11.8	12.7
Ta/Yb	0.04	0.05	0.05	0.04	0.04	0.04	0.06	0.03	0.06	0.12	0.05	0.05	0.05
Ba/La	15	25	21.5	29.5	22.5	23.2	19.1	21.6	17.1	46.9	18.9	26.7	36
U/Th	0.31	0.7	0.69	0.75	0.69	0.75	0.64	0.35	0.69	0.73	0.76	0.87	0.69

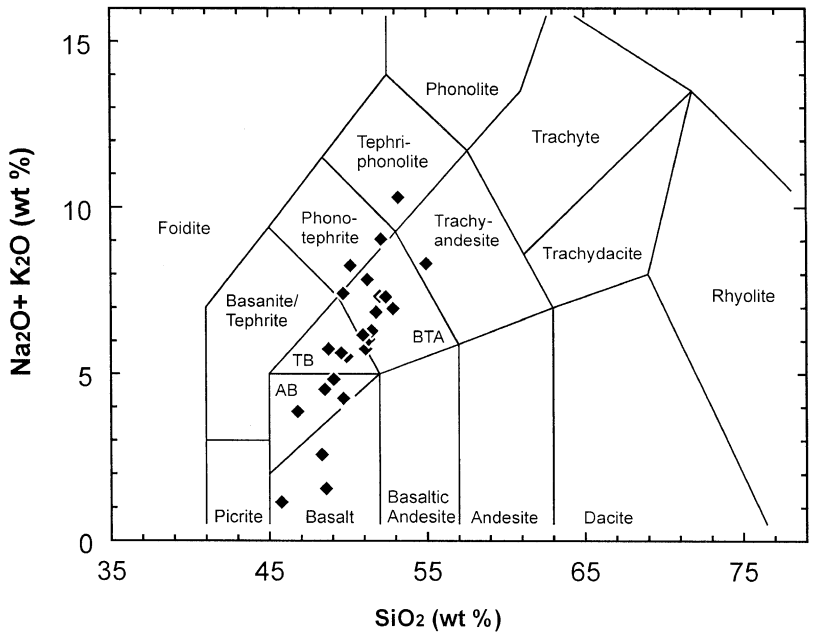

Fig. 5. Total alkali vs. SiO_2 biaxial plot (TAS plot) showing the compositions of the investigated samples ranging from basalt through trachybasalt to trachyandesite. One sample plots in the tephriphonolite field.

wide range of mg# (31–79) that are calculated using a molecular $Fe^2/(Fe^2 + Fe^3)$ set at 0.15, a common ratio in potassic igneous rocks (Müller et al., 1992). The rocks (Figs. 5 and 6) are characterized by high

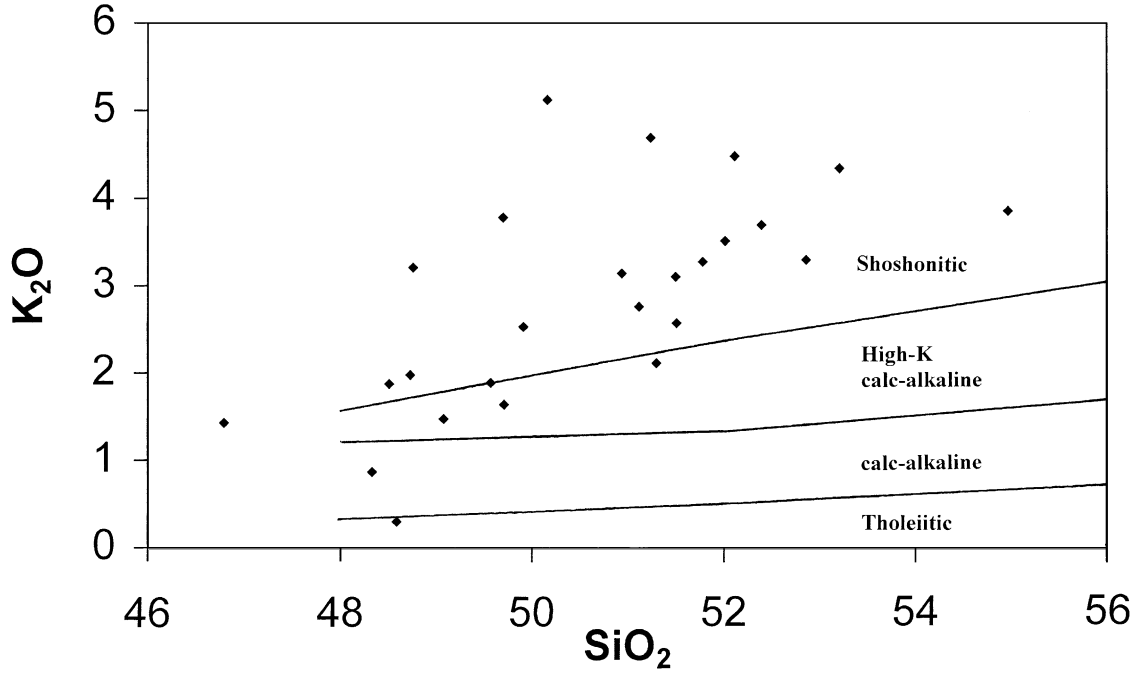

Fig. 6. K_2O vs. SiO_2 biaxial plot, after Peccerillo and Taylor (1976), illustrating the potassic compositions of investigated samples.

K_2O contents (up to 4.68 wt.%), high average K_2O/Na_2O ratios (0.8), and high average Ce/Yb ratios (14.1), which are typical of high-K igneous rocks transitional to shoshonites (Pearce, 1982; Müller et al., 1992). However, based on their geochemistry, the rocks cannot be classified as shoshonites *sensu stricto* (Morrison, 1980) as suggested by previous workers (e.g., Moyle et al., 1990). The relatively high CaO concentrations of the rocks (up to 17.67 wt.%) reflect their derivation from fertile upper mantle material (Schmidt et al., 2000) that was metasomatically enriched during subduction processes (Kennedy et al., 1990). The high LILE (e.g., Rb, Sr, Ba up to 186, 1461, and 760 ppm, respectively), low LREE (e.g., La < 20.3 ppm, Ce < 38.4 ppm), and very low HFSE concentrations (e.g., Zr < 132 ppm, Nb < 4.2 ppm, Hf < 3.7 ppm) are typical for potassic igneous rocks from oceanic (island) arc settings (cf. Müller et al., 1992). The oceanic (island) arc setting is confirmed by plotting the data on the Zr vs. Y biaxial and the La–$TiO_2/100$–Hf × 10 triangular discrimination diagrams (Figs. 7 and 8).

Most samples are *hypersthene*-normative and only four, with high total alkali contents (> 5.64 wt.%), are *nepheline*-normative (i.e., samples 7, 22, 23, and 25). Although previous studies by Kennedy et al. (1990) suggested that the Luise lavas may be separated into primitive and relatively evolved groups, with two distinct fractionation trends, this is not confirmed by our data. For comparison, we plotted the regional data from the Luise, Huniho, Wurtol and Londolovit volcanoes on the SiO_2 vs. Al_2O_3 and

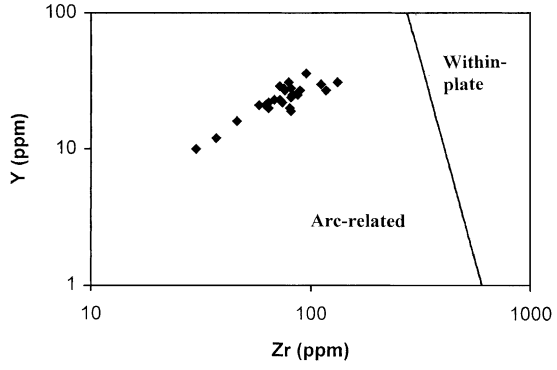

Fig. 7. Y vs. Zr biaxial geochemical discrimination diagram indicating the subduction-arc features of the rocks from Lihir Island.

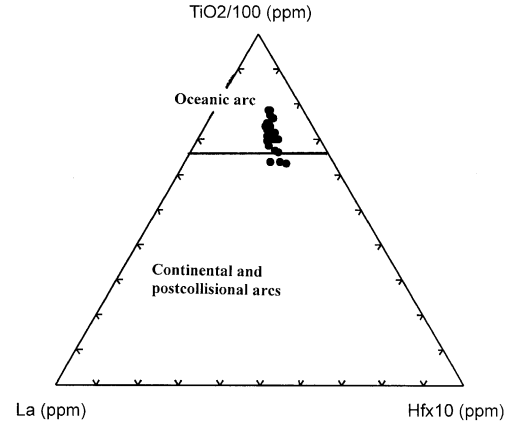

Fig. 8. $TiO_2/100$–La–Hf × 10 triangular discrimination diagram showing the oceanic (island) arc features of the rocks from Lihir Island.

SiO_2 vs. CaO biaxial plots used by Kennedy et al. (1990). Most samples plot along the fractionation trend outlined by the arrows in Fig. 9a and b, respectively, suggesting that the melts from Londolovit, Huniho, Wurtol and Luise volcanoes are related to a single common parental magma, probably derived from an underlying magma chamber. This fractionation trend represents the "evolved trend" of Kennedy et al. (1990). "Outliers" are restricted to three olivine–clinopyroxene cumulates (i.e., samples 1, 2, 6) and two samples with moderate potassic (biotite) alteration (i.e., samples 23, 25). The "primitive trend" mentioned by Kennedy et al. (1990) is not evident in our data set. Furthermore, all samples, including the cumulates, plot along a single fractionation trend on a MgO vs. Al_2O_3 biaxial diagram (Fig. 9b).

Recent studies on mantle-derived rocks by Gregoire et al. (2000) imply that the trace elements Sr, Y, Zr, Th and LREE are mainly contained in clinopyroxene, while the HREE, such as Yb and Lu, are sited in olivine. The phonolite (sample 22) has very low Ho contents (0.68 ppm), but relatively high Th (2.2 ppm) when compared to the SiO_2-saturated samples. All samples have similar Ba/Zr ratios of 2.5–4.2, which are consistent with their fresh nature. Only the phonolite (sample 22) and one of the two samples with moderate potassic alteration from Wurtol volcano (i.e., sample 25) have higher Ba/Zr ratios (i.e., 9.4 and 6.7, respectively).

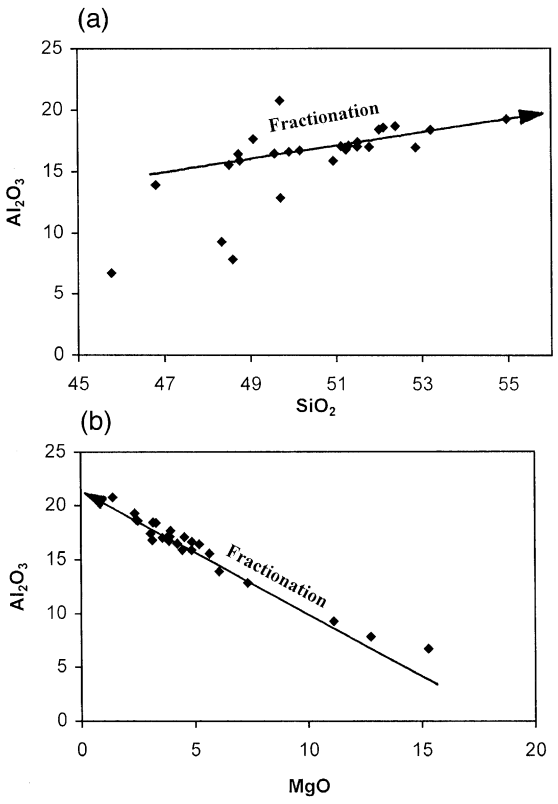

Fig. 9. (a) SiO_2 vs. Al_2O_3 biaxial diagram showing the fractionation trend of the rocks from Huniho, Wurtol, Luise and Londolovit volcanoes suggesting their derivation from a single parental magma chamber beneath the island. Outliers are the augite–olivine cumulates (samples 1, 2, and 6); (b) MgO vs. Al_2O_3 biaxial diagram showing the fractionation trend of the rocks from Huniho, Wurtol, Luise, and Londolovit volcanoes suggesting their derivation from a single parental magma chamber beneath the island. Even the augite–olivine cumulates fall on this fractionation trend.

As previously pointed out by De Astis et al. (2000), both a fluid-rich and a sediment-related mantle metasomatism can produce potassic melts in subduction zones. Importantly, the work of Patino et al. (2000) suggests that Ba/La and U/Th ratios in volcanics may be used to deduce the participation of sedimentary material during melting processes in the mantle wedge above a subduction zone. According to their data, high Ba/La and U/Th ratios (i.e., > 70 and > 0.65, respectively) indicate distinct sedimentary input. However, the rocks from Lihir Island are characterized by low average Ba/La and U/Th ratios (i.e., 21.4 and 0.65, respectively) thus indicating that there has been negligible sediment input into their mantle source during subduction.

6. Thermobarometry and oxygen fugacity of the igneous rocks

Temperature estimates based on the Fe–Mg exchange of coexisting titanomagnetite–olivine pairs in a trachybasalt and a monzodiorite from Londolovit volcano yielded 893–965°C using the calibration of Ballhaus et al. (1991). Similar temperatures (i.e., 920–930°C) were calculated for chromian spinel and olivine xenocrysts in an olivine basalt from Huniho volcano (Table 4). Thermometry using the Ti contents of Mg-hastingsite in trachyandesites from Luise and Huniho volcano lay in the same range. Temperatures calculated using the calibration of Colomby (1988) varied from 865°C to 940°C (cf. Table 3), a range which was also reproduced by the semi-quantitative Ti in hornblende geothermometer of Ernst and Liu (1998). Distinctly lower temperatures of 780–840°C were obtained using coexisting titanomagnetite and olivine in cumulates from Londolovit and Luise volcanoes by applying the olivine–spinel geothermometer of (Ballhaus et al., 1991; Table 4).

The pressure dependence of the Al content of magmatic amphibole can be estimated by means of several calibrations (e.g., Hammarstrom and Zen, 1986; Hollister et al., 1987; Johnson and Rutherford, 1989; Schmidt, 1992), which, however, only deliver maximum pressures for the crystallisation of the hornblende and, furthermore, were set up for different temperatures. A temperature correction for this geobarometer was proposed by Anderson and Smith (1995). An application of their calibration to trachyandesites from Lihir island yields maximum pressures of 0.5 kbar at temperatures of 865–940°C (cf. Table 3), thus pointing to a very shallow level of crystallisation. Similar results are obtained using the clinopyroxene geobarometer of Nimis (1995), which is based on crystal–structural modeling. For the volcanics, as well as the hypabyssal intrusive rocks, maximum pressures of about 0.5 kbar were calculated, while the cumulates revealed higher pressures of up to 1.7 kbar.

For samples with coexisting chromian spinel and olivine, the oxygen fugacity within the melt can be

determined using the oxygen geobarometer of Ballhaus et al. (1991), which results in Δf_{O_2} values of 2.04–2.27 log units above the FMQ buffer (Fig. 10). Similarly, high oxygen fugacities were determined for metasomatic mantle xenoliths from the TUBAF seamount, about 5 km south of Lihir (Franz and Wirth, 2000; Franz et al., 2001). As the oxygen geobarometer of Ballhaus et al. (1991) is restricted to spinels with TiO_2 contents of < 1 wt.% (C. Ballhaus, personal communication, 2000), the oxygen fugacity of titanomagnetite-bearing intrusive rocks was determined with the QUILF program of Lindsley and Frost (1992; version of Andersen et al., 1993). The application of this program yielded elevated oxygen fugacities of 1.43–2.67 log units above the FMQ buffer for volcanics (Müller et al., 2000) and of 3.84–4.8 log units above the FMQ buffer for the cumulates (Table 4). Subduction-derived calc-alkaline rocks (Frost and Lindsley, 1992) generally have higher oxygen fugacities (Δf_{O_2} of 1–2 log units above that of FMQ) than tholeiites (generally about 1 log unit below FMQ). The high f_{O_2} of the investigated samples from Lihir Island are consistent with empirical observations by Ballhaus (1993) that basaltic rocks from oceanic island arcs are commonly formed under very high f_{O_2} conditions that can be up to $+3$ log units above FMQ. Parkinson and Arculus (1999) noted that the maximum f_{O_2} of fertile mantle is unlikely to be $+2$ log units above FMQ. These authors proposed decompression melting in the mantle wedge as the key process responsible for the high f_{O_2} observed in many oceanic island arc settings. The high oxygen fugacities of the cumulates may be explained by influx of water to a shallow magma chamber beneath Lihir Island, as documented at Jorullo volcano in Mexico (cf. Luhr and Carmichael, 1985).

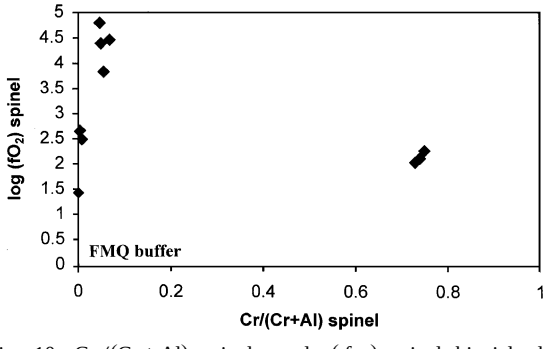

Fig. 10. $Cr/(Cr+Al)$ spinel vs. $\log(f_{O_2})$ spinel biaxial plot illustrating the high oxygen fugacities of the rocks from Lihir Island.

7. Discussion

Lithosphere above subduction zones is commonly assumed to be more oxidized than other mantle regimes (W.R. Taylor, personal communication, 1992) because of its infiltration by slab-derived fluids generated from dehydration and decarbonation reactions (Arculus, 1985; Haggerty, 1990; Lange and Carmichael, 1990; Mysen and Wheeler, 2000). The dissociation of H_2O and the release of H^+ should enrich the system in oxygen at an early stage before the onset of partial melting (Abdel-Rahman, 1994). However, recent experimental studies by Moore et al. (1995) indicate that dissolved water does not measurably affect the redox state of iron in natural melts. Therefore, the high oxygen fugacities, which are commonly recorded in water-rich magmas (e.g., Lange and Carmichael, 1990), are probably a record of other processes that have imposed a high oxygen fugacity (f_{O_2}) upon the melt, and are not a reflection of the amount of dissolved water (Moore et al., 1995). Parkinson and Arculus (1999) suggest that the ultimate source of the oxygen that oxidises the mantle wedge might be derived from the subducted slab. However, they note that it is still not clear whether this oxidising agent is a solute-rich hydrous fluid or a water-bearing silicate melt.

At high values of f_{O_2}, iron is partially transformed into Fe^{3+} and oxide minerals such as magnetite crystallize in preference to Fe^{2+}-bearing silicate minerals (Haggerty, 1990). The high alkali content of potassic melts increases their Fe^{3+}/Fe^{2+} ratios, thus resulting in a higher oxygen fugacity (D. Wyborn, personal communication, 1995). A high f_{O_2} of the magmas, as indicated by significant concentrations of magnetite (> 5 vol.%) in their crystallized products, seems to favour precipitation of large quantities of gold (Sillitoe, 1979). Hence, it is no coincidence that the potassic igneous rocks of Lihir Island are characterized by appreciable magnetite.

At constant temperatures, as f_{O_2} increases, the concentration of dissolved sulphide (S^{2-}) in the melt

decreases, while the dissolved sulphate (SO_4^{2-}) increases (Carmichael and Ghiorso, 1986), thus minimising the loss of precious metals into sulphide phases (Richards, 1995). Potassic magmas may contain sulphate minerals (e.g., anhydrite) and are, therefore, considerably more oxidized than, for example, tholeiites (Haggerty, 1990). The abundance of late anhydrite veins and anhydrite-sealed breccias in the Ladolam gold deposit is consistent with a high f_{O_2} for these potassic rocks, although the latter are also due to the influx of seawater—a special condition of Ladolam (cf. Müller et al., 2001).

An important prerequisite for the hydrothermal extraction of Au from a magma is that removal of chalcophile elements from the melt by sulphide–liquid segregation should not occur before volatile saturation (Candela, 1992; Richards, 1995). This condition may be achieved by suppression of sulphur saturation through a high oxidation state of the magma, thus promoting the presence of sulphur as sulphate, not sulphide, within the melt (Candela, 1992; Richards, 1995).

Importantly, Ballhaus (1993) documented a positive correlation between the calculated f_{O_2} of igneous rocks and their volatile contents. Studies on the potassic host rocks of the copper–gold deposits at Bajo de la Alumbrera, Argentina, and Grasberg, Indonesia, and the gold deposit at Porgera, Papua New Guinea, also reveal the presence of high f_{O_2} and high halogen contents (Müller and Groves, 2000). Hence, both the high f_{O_2} of the investigated samples (Fig. 10) and their high halogen contents, as reflected in mica compositions (Table 5), may reflect the high mineralization potential of the former alkaline melts beneath Lihir Island.

The fact that Cl and F in rock-forming minerals generally occupy hydroxyl sites of hydrous minerals, in particular phlogopites (Fuge et al., 1986; Foley, 1989), led to the detailed study of halogen contents of mica specimens from Lihir Island (Table 5). The investigated micas are generally characterized by highly elevated halogen concentrations (Table 5), which are consistent with data from other world-class gold $\pm$ copper deposits hosted by potassic igneous rocks at Grasberg, Northparkes (Goonumbla) and Porgera (cf. Müller and Groves, 2000).

Previous studies have established the important role of halogens (Cl, F) for the transport of metals in ore deposits related to igneous rocks (e.g., Webster, 1992; Stanton, 1994). Chlorine largely controls the abundances of chlorophile ore and associated elements (e.g., Fe, Na, K, Cu) in saline aqueous fluids that exsolve from magma (Webster, 1992), and it also increases PGE solubilities in both sulphide and silicate melts (Peach et al., 1994). The strong affinity of the halogens for potassium, particularly in micas, can be explained in terms of their electronic configurations (Cocco et al., 1972).

Fluorine contents increase regularly from tholeiites to potassic basalts (Aoki et al., 1981), and F is a common element in potassic magmas (Edgar and Charbonneau, 1991). Experimental studies by Vukadinovic and Edgar (1993) suggest that F, in contrast to Cl (see Magenheim et al., 1995), behaves as a mantle-compatible element. Under mantle conditions, F tends to remain in the solid phases rather than partition into the first melt increments during partial melting (Vukadinovic and Edgar, 1993). During crystallization, F is partitioned into the hydrous phenocrysts rather than remaining in the melt (Edgar et al., 1994). In accord with this, Kesler et al. (1975) have shown that the average whole-rock halogen contents of potassic intrusions (> 2 wt.% K_2O) are higher (240 ppm Cl, 620 ppm F) than those for non-potassic (< 2 wt.% K_2O) intrusions (160 ppm Cl, 380 ppm F). Recent studies have shown that alkaline magmas such as potassic melts are characteristically enriched in halogens (e.g., Foley et al., 1986; Foley, 1989; Zhang et al., 1995), suggesting that the strongest Cl enrichments of magmatic–hydrothermal fluids, and ore metals complexed with Cl, occur in fluids exsolved from magmas that are relatively enriched in K_2O (Webster, 1992). Experimental studies on alkaline melts suggest that Cl solubility is a strong function of melt composition and high solubilities can be expected in alkali-rich, low silica activity compositions (Signorelli and Carroll, 2000). Hence, many gold deposits tend to be associated with the more volatile-rich potassic and calc-alkaline magmas (Spooner, 1993), where a magmatic connection is indicated (Richards, 1995).

8. Conclusions

(1) Lihir Island consists of five volcanoes comprising high-K igneous rocks, one of them hosting

Ladolam, one of the largest epithermal gold deposits to be discovered. The rocks range from porphyritic trachybasalts through trachyandesites to latites which, in places, are cut by monzodiorite stocks. More rarely, phonolites and olivine–clinopyroxene cumulates occur.

(2) The volcanic rocks range from primitive to relatively evolved compositions, as reflected by their contents of SiO_2 (45.8–55.0 wt.%) and MgO (1.4–15.3 wt.%), and variable concentrations of mantle-compatible elements (130–328 ppm V, 1–186 ppm Ni). Their high K_2O contents (up to 4.7 wt.%), high average K_2O/Na_2O ratios (0.8), and high average Ce/Yb ratios (14) are typical for high-K igneous rocks transitional to shoshonites.

(3) Partial melting of subduction-modified upper mantle beneath Lihir Island was triggered by adiabatic decompression melting linked to extensional structures related to back-arc rifting of the Manus Basin. Despite their derivation in a back-arc setting, the high LILE (Rb, Sr, Ba up to 186, 146, and 760 ppm, respectively), low LREE (La < 20.3 ppm, Ce < 38.4 ppm), and very low HFSE concentrations (Zr < 132 ppm, Nb < 4.2 ppm, Hf < 3.7 ppm) of the investigated samples are typical for potassic igneous rocks from oceanic (island) arc settings (cf. Müller et al., 1992).

(4) The low average Ba/La and U/Th ratios (21.4 and 0.65, respectively) of the rocks suggest only a minor sediment input to their mantle source during subduction.

(5) Electron microprobe analyses of mica phenocrysts from the Lihir rocks reveal very high halogen concentrations. Primary (magmatic) micas can be classified as phlogopites with very high F (up to 5.6 wt.%) and elevated Cl contents (< 0.08 wt.%). In contrast, secondary (hydrothermal) micas from samples that underwent potassic alteration have very low F (< 0.08 wt.%), but very high Cl concentrations (up to 0.15 wt.%). The halogen concentrations of the rocks are higher, but consistent with, those from high-K igneous rocks hosting the world-class copper ± gold deposits at Goonumbla, Australia, Grasberg, Indonesia, and Porgera, Papua New Guinea.

(6) Lihir Island volcanic and hypabyssal rocks, which crystallized near the surface ($P \leq 0.5$ kbar) at temperatures ranging between 865°C and 965°C, are characterized by very high oxygen fugacities (f_{O_2} ranging between 2.04 and 3.94 log units above that of the FMQ buffer). The P–T estimates for cumulates indicate slightly higher pressures of crystallisation ($P \leq 1.7$ kbar) at temperatures of 780–840°C. Their oxygen fugacities were even higher (i.e., 3.8–4.1 log units above that of the FMQ buffer), which may be due to interaction of the magma with ground or seawater in a shallow magma chamber. Although high oxygen fugacities have been indirectly inferred for other major alkaline rock-hosted gold deposits, based on their abundant magmatic magnetite and anhydrite contents, this is the first time that the f_{O_2} of alkaline host rocks of a major gold deposit has been precisely defined. The high f_{O_2} was essential in the genesis of epithermal gold mineralization at Ladolam. High oxygen fugacities of parental melts delay early crystallization of sulphides in the melt thus promoting the presence of sulphur as sulphate, rather than sulphide; this is important since chalcophile metals such as gold and copper preferentially partition into sulphide phases resulting in depletion in the melt during fractionation.

Acknowledgements

Chris Ballhaus (Münster), Ron Frost (Canberra) and Don Lindsley (Stony Brook, NY) are thanked for their advice on the f_{O_2} determinations. D.M. is very grateful to Michael Kande and Mannie Mehu (both Lihir Gold) for their support and help during field work. Thanks are also due to Alexander Konschak (Freiberg) for the preparation of sample powders and to Klaus Becker, Freiberg, for his assistance with microprobe analyses. This study has been financially supported by the German Research Foundation (DFG grants MU 1619/1-1 and 1619/1-2 to D.M.) and by Lihir Gold. Many thanks are due to Richard Sillitoe (London) and an anonymous reviewer for their critical comments on the manuscript.

References

Abdel-Rahman, A.M., 1994. Nature of biotites from alkaline, calc-alkaline and peraluminous magmas. J. Petrol. 35, 525–541.

Andersen, D.J., Lindsley, D.H., Davidson, P.M., 1993. QUILF: a

Pascal program to assess equilibria among Fe–Mg–Mn–Ti oxides, pyroxenes, olivine, and quartz. Comput. Geosci. 19, 1333–1350.

Anderson, J.L., Smith, D.R., 1995. The effects of temperature and f_{O_2} on the Al-in-hornblende barometer. Am. Mineral. 80, 549–559.

Andrew, R.L., 1995. Porphyry copper–gold deposits of the Southwest Pacific. Min. Eng. 47, 33–38.

Aoki, K., Ishiwaka, K., Kanisawa, S., 1981. Fluorine geochemistry of basaltic rocks from continental and oceanic regions and petrogenetic application. Contrib. Mineral. Petrol. 76, 53–59.

Arculus, R.J., 1985. Oxidation status of the mantle: past and present. Annu. Rev. Earth Planet. Sci. 13, 75–95.

Ballhaus, C., 1993. Redox states of lithospheric and asthenospheric upper mantle. Contrib. Mineral. Petrol. 114, 331–348.

Ballhaus, C., Berry, R.F., Green, D.H., 1991. High pressure experimental calibration of the olivine–orthopyroxene–spinel oxygen geobarometer: implications for the oxidation state of the upper mantle. Contrib. Mineral. Petrol. 107, 27–40.

Beane, R.E., Titley, S.R., 1981. Porphyry copper deposits: part II. Hydrothermal alteration and mineralization. Econ. Geol. 75th Anniv., 235–269.

Candela, P.A., 1992. Controls on ore metal ratios in granite-related ore systems: an experimental and computational approach. Trans. R. Soc. Edinburgh: Earth Sci. 83, 317–326.

Carmichael, I.S.E., Ghiorso, M.S., 1986. Oxidation–reduction relations in basic magma: a case for homogeneous equilibria. Earth Planet. Sci. Lett. 78, 200–210.

Cocco, G., Fanfani, L., Zanazzi, P.F., 1972. Potassium. In: Wedepohl, K.H. (Ed.), Handbook of Geochemistry, vol. II-2, Springer-Verlag, Berlin.

Coleman, P.J., Kroenke, L.W., 1981. Subduction without volcanism in the Solomon Island arc. Geo-Mar. Lett. 1, 129–134.

Colomby, A., 1988. Métamorphisme et géochemie des roches mafiques des Alpes ouest-centrales (géoprofil Viège–Domodossola–Locarno). PhD thesis, University Lausanne (CH), 216 pp.

Corbett, G.J., 1999. Comments on the structural controls and styles of gold mineralization in the Minifie pit, Lihir Island. Unpl. Report to Lihir Management Company: 15 pp.

Davies, R.M., Ballantyne, G.H., 1987. Geology of the Ladolam gold deposit, Lihir Island, Papua New Guinea. Pac. Rim Conf. 87, 943–949.

De Astis, G., Peccerillo, A., Kempton, P.D., La Volpe, L., Wu, T.W., 2000. Transition from calc-alkaline to potassium-rich magmatism in subduction environments: geochemical and Sr, Nd, Pb isotopic constraints from the island of Vulcano (Aeolian arc). Contrib. Mineral. Petrol. 139, 684–703.

Edgar, A.D., Charbonneau, H.E., 1991. Fluorine-bearing phases in lamproites. Mineral. Petrol. 44, 125–149.

Edgar, A.D., Lloyd, F.E., Vukadinovic, D., 1994. The role of fluorine in the evolution of ultrapotassic magmas. Mineral. Petrol. 51, 173–193.

Ernst, W.G., Liu, J., 1998. Experimental phase equilibrium study of Al- and Ti-contents of calcic amphibole in MORB—a semiquantitative thermobarometer. Am. Mineral. 83, 952–969.

Foley, S.F., 1989. Experimental constraints on phlogopite chemistry in lamproites: 1. The effect of water activity and oxygen fugacity. Eur. J. Mineral. 1, 411–426.

Foley, S.F., Taylor, W.R., Green, D.H., 1986. The role of fluorine and oxygen fugacity in the genesis of the ultrapotassic rocks. Contrib. Mineral. Petrol. 94, 183–192.

Franz, L., Wirth, R., 2000. Spinel inclusions in olivine of peridotite xenoliths from TUBAF seamount (Bismarck Archipelago/Papua New Guinea): evidence for the thermal and tectonic evolution of the oceanic lithosphere. Contrib. Mineral. Petrol. 140, 283–295.

Franz, L., Becker, K.-P., Kramer, W., Herzig, P.M., 2001. Veined mantle xenoliths from the metasomatic fore-arc wedge of the Bismarck Microplate (Papua New Guinea)—petrological and geochemical consequences and extent of slab-induced hydrous metasomatism. J. Petrol., in press.

Frost, B.R., Lindsley, D.H., 1992. Equilibria among Fe–Ti oxides, pyroxenes, olivine, and quartz: part II. Application. Am. Mineral. 77, 1004–1020.

Fuge, R., Andrews, M.J., Johnson, C.C., 1986. Chlorine and iodine, potential pathfinder elements in exploration geochemistry. Appl. Geochem. 1, 111–116.

Gregoire, M., Moine, B.N., O'Reilly, S.Y., Cottin, J.Y., Giret, A., 2000. Trace element residence and partitioning in mantle xenoliths metasomatized by highly alkaline, silicate- and carbonate-rich melts (Kerguelen Islands Indian Ocean). J. Petrol. 41, 477–509.

Haggerty, S.E., 1990. Redox state of the continental lithosphere. In: Menzies, M.A. (Ed.), Continental Mantle. Clarendon Press, Oxford, pp. 87–109.

Hammarstrom, J.M., Zen, E-an., 1986. Aluminium in hornblende: an empirical igneous geobarometer. Am. Mineral. 71, 1297–1313.

Hollister, L.S., Grissom, G.C., Peters, E.K., Stowell, H.H., Sisson, V.B., 1987. Confirmation of the empirical correlation of Al in hornblende with pressures of solidification of calc-alkaline plutons. Am. Mineral. 72, 231–239.

Hoogvliet, H., 1993. The Ladolam gold deposit–at least two major events. Aust. J. Min., September, 20.

Jarosewich, E., Nelen, J.A., Norberg, J.A., 1980. Reference samples for electron microprobe analysis. Geostand. Newsl. 4, 43–47.

Johnson, M.C., Rutherford, M.J., 1989. Experimental calibration of the aluminium-in-hornblende geobarometer with application to Long Valley Caldera (California) volcanic rocks. Geology 17, 837–841.

Kennedy, A.K., Grove, T.L., Johnson, R.W., 1990. Experimental and major element constraints on the evolution of lavas from Lihir Island, Papua New Guinea. Contrib. Mineral. Petrol. 104, 722–734.

Kesler, S.E., Issigonis, M.J., Brownlow, A.H., Damon, P.E., Moore, W.J., Northcote, K.E., Preto, V.A., 1975. Geochemistry of biotites from mineralized and barren intrusive systems. Econ. Geol. 70, 559–567.

Komyshan, P., 1999. Geological interpretations of Lihir Island. CSA, unpublished company report R8.99, 40 pp.

Lange, R.A., Carmichael, I.S.E., 1990. Hydrous basaltic andesites

associated with minette and related lavas in Western Mexico. J. Petrol. 31, 1225–1259.

Leake, B.W., Wooley, A.R., Arps, C.E.S., Birch, W.D., Gilbert, M.C., Grice, J.D., Hawthorne, F.C., Kato, A., Kisch, H.J., Krivovichev, V.G., Linthout, K., Laird, J., Mandarino, J., Maresch, W.V., Nickel, E.H., Rock, N.M.S., Schumacher, J.C., Smith, D.C., Stephenson, N.C.N., Ungaretti, L., Whittaker, E.J.W., Youzhi, G., 1997. Nomenclature of amphiboles. Report of the subcommittee on amphiboles of the International Mineralogical Association Commission on new minerals and mineral names. Eur. J. Mineral. 9, 623–651.

Licence, P.S., Terril, J.E., Fergusson, L.J., 1987. Epithermal gold mineralisation, Ambittle Island, Papua new Guinea. Pac. Rim Conf. 87, 273–278.

Lindsley, D.H., 1983. Pyroxene thermometry. Am. Mineral. 68, 477–493.

Lindsley, D.H., Frost, B.R., 1992. Equilibria among Fe–Ti oxides, pyroxenes, olivine, and quartz: part I. Theory. Am. Mineral. 77, 987–1003.

Lopez, D.L., Williams, S.N., 1993. Catastrophic volcanic collapse: relation to hydrothermal processes. Science 260, 1794–1796.

Luhr, J.F., Carmichael, I.S.E., 1985. Jorullo Volcano, Michoacan, Mexico: the earliest stages of fractionation in calc-alkaline magmas. Contrib. Mineral. Petrol. 90, 142–161.

Magenheim, A.J., Spivack, A.J., Michael, P.J., Gieskes, J.M., 1995. Chlorine stable isotope composition of the oceanic crust: implications for Earth's distribution of chlorine. Earth Planet. Sci. Lett. 131, 427–432.

McInnes, B.I.A., Cameron, E.M., 1994. Carbonated, alkaline hybridizing melts from a sub-arc environment: mantle wedge samples from the Tabar–Lihir–Tanga–Feni arc, Papua New Guinea. Earth Planet. Sci. Lett. 122, 125–141.

Moore, G., Righter, K., Carmichael, I.S.E., 1995. The effect of dissolved water on the oxidation state of iron in natural silicate liquids. Contrib. Mineral. Petrol. 120, 170–179.

Morimoto, N., Fabries, J., Ferguson, A.K., Ginzburg, I.V., Ross, M., Seifert, F.A., Zussman, J., Aoki, K., Gottardi, G., 1988. Nomenclature of pyroxenes. Mineral. Petrol. 39, 55–76.

Morrison, G.W., 1980. Characteristics and tectonic setting of the shoshonite rock association. Lithos 13, 97–108.

Moyle, A.J., Doyle, B.J., Hoogvliet, H., Ware, A.R., 1990. Ladolam gold deposit, Lihir Island. In: Hughes, F.E. (Ed.), Geology of the Mineral Deposits of Australia and Papua New Guinea. Australasian Institute of Mining and Metallurgy, Parkville, Australia, pp. 1793–1805.

Müller, D., Groves, D.I., 1993. Direct and indirect associations between potassic igneous rocks, shoshonites and gold–copper deposits. Ore Geol. Rev. 8, 383–406.

Müller, D., Groves, D.I., 2000. Potassic Igneous Rocks and Associated Gold–Copper Mineralization. 3rd edn. Springer-Verlag, Berlin, 252 pp.

Müller, D., Rock, N.M.S., Groves, D.I., 1992. Geochemical discrimination between shoshonitic and potassic volcanic rocks in different tectonic settings: a pilot study. Mineral. Petrol. 46, 259–289.

Müller, D., Franz, L., Herzig, P.M., 2000. Alkaline rocks hosting the epithermal gold mineralization at Lihir Island, Papua New Guinea. Beih. Eur. J. Mineral. 12, 133.

Müller, D., Kaminski, K., Uhlig, S., Graupner, T., Herzig, P.M., Hunt, S., 2001. The transition from porphyry- to epithermal-style gold mineralization at Ladolam, Lihir Island, Papua New Guinea. Miner. Deposita (in press).

Mysen, B.O., Wheeler, K., 2000. Alkali aluminosilicate-saturated aqueous fluids in the Earth's upper mantle. Geochim. Cosmochim. Acta 64, 4243–4256.

Nimis, P., 1995. A clinopyroxene geobarometer for basaltic systems based on crystal-structure modeling. Contrib. Mineral. Petrol. 121, 115–125.

Parkinson, I.J., Arculus, R.J., 1999. The redox state of subduction zones: insights from arc-peridotites. Chem. Geol. 160, 409–423.

Patino, L.C., Carr, M.J., Feigenson, M.D., 2000. Local and regional variations in Central American arc lavas controlled by variations in subducted sediment input. Contrib. Mineral. Petrol. 138, 265–283.

Peach, C.L., Mathez, E.A., Keays, R.R., Reeves, S.J., 1994. Experimentally determined sulphide melt–silicate melt partition coefficients for iridium and palladium. Chem. Geol. 117, 361–377.

Pearce, J.A., 1982. Trace element characteristics of lavas from destructive plate boundaries. In: Thorpe, R.S. (Ed.), Andesites. Wiley, New York, pp. 525–548.

Peccerillo, A., Taylor, S.R., 1976. Geochemistry of Eocene calc-alkaline volcanic rocks from the Kastomonon area, northern Turkey. Contrib. Mineral. Petrol. 58, 63–81.

Richards, J.P., 1995. Alkalic-type epithermal gold deposits—a review. In: Thompson, J.F.H. (Ed.), Magmas, Fluids, and Ore Deposits. Mineral. Assoc. Can., Short Course Ser., vol. 23, pp. 367–400.

Rytuba, J.J., McKee, E.H., Cox, D., 1993. Geochronology and geochemistry of the Ladolam gold deposit, Lihir island, and gold deposits and volcanoes of Tabar and Tatau, Papua New Guinea. U. S. Geol. Surv. Bull. 2039, 119–126.

Schmidt, M.W., 1992. Amphibole composition in tonalite as a function of pressure: an experimental calibration of the Al-in-hornblende barometer. Contrib. Mineral. Petrol. 110, 304–310.

Schmidt, G., Palme, H., Kratz, K.L., Kurat, G., 2000. Are highly siderophile elements (PGE, Re and Au) fractionated in the upper mantle of the Earth? New results on peridotites from Zabargad. Chem. Geol. 163, 167–188.

Signorelli, S., Carroll, M.R., 2000. Solubility and fluid-melt partitioning of Cl in hydrous phonolitic melts. Geochim. Cosmochim. Acta 64, 2851–2862.

Sillitoe, R.H., 1979. Some thoughts on gold-rich porphyry copper deposits. Miner. Deposita 14, 161–174.

Sillitoe, R.H., 1994. Erosion and collapse of volcanoes: causes of telescoping in intrusion-centered ore deposits. Geology 22, 945–948.

Sillitoe, R.H., 1997. Characteristics and controls of the largest porphyry Cu–Au and epithermal Au deposits in the circum-Pacific region. Aust. J. Earth Sci. 44, 373–388.

Spooner, E.T.C., 1993. Magmatic sulphide/volatile interaction as a mechanism for producing chalcophile element enriched,

Archean Au-quartz hydrothermal ore fluids. Ore Geol. Rev. 7, 359–379.

Stanton, R.L., 1994. Ore elements in arc lavas. Oxford Monographs in Geology and Geophysics, vol. 29, Clarendon Press, New York, 391 pp.

Steward, W.D., Sandy, M.J., 1988. Geology of New Ireland and Djaul Islands, northeast Papua New Guinea. In: Marlow, M.S., Dadisman, S.V., Exton, N.F. (Eds.), Geology and offshore resources of Pacific island arcs—New Ireland and Manus region, Papua New Guinea. Circum-Pacific Council for Energy and Mineral Resources. Earth Sci. Ser., vol. 9, pp. 12–30.

Taylor, B., 1979. Bismarck Sea: evolution of a back arc basin. Geology 7, 171–174.

Voight, B., Elsworth, D., 1997. Failure of volcano slopes. Geotechnique 47, 1–31.

Vukadinovic, D., Edgar, A.D., 1993. Phase relations in the phlogopite–apatite system at 20 kbar—implications for the role of fluorine in mantle melting. Contrib. Mineral. Petrol. 114, 247–254.

Wallace, D.A., Johnson, R.W., Chappell, B.W., Arculus, R.J., Perfit, M.R., Crick, I.H., 1983. Cainozoic volcanism of the Tabar, Lihir, Tanga, and Feni islands, Papua New Guinea: geology, whole-rock analyses, and rock-forming mineral compositions. Bureau of Mineral Resources, Australia, BMR Rep 243.

Webster, J.D., 1992. Water solubility and chlorine partitioning in Cl-rich granitic systems: effects of melt composition at 2 kbar and 800°C. Geochim. Cosmochim. Acta 56, 679–687.

Zhang, M., Suddaby, P., Thompson, R.N., Thirlwall, M.F., Menzies, M.A., 1995. Potassic volcanic rocks in NE China: geochemical constraints on mantle source and magma genesis. J. Petrol. 36, 1275–1303.